Available online at www.sciencedirect.com

jmr&t Journal of Materials Research and Technology

journal homepage: www.elsevier.com/locate/jmrt

Construction and parameter optimization of LPBF-NiTi alloy bionic superhydrophobic surface based on laser processing

Yingchun Qi [a], Pengwei Sha [a,b], Kun Yang [c], Bochao Jia [b], Zezhou Xu [a,b,**], Yanan Yang [a,b], Yunting Guo [a,b], Lunxiang Li [b], Qing Cao [a,b], Tingting Zou [d], Jianjun Yang [d], Zhenglei Yu [a,b,*], Zhengzhi Mu [a,b]

[a] Key Laboratory of Bionic Engineering, Ministry of Education, Jilin University, 5988, Renmin Street, Changchun 130025, China

[b] Weihai institute for Bionic, Jilin University, Weihai, 264402, China

[c] Basic Education College of Aviation University of Air Force, Changchun, 130000, China

[d] GPL Photonics Laboratory, State Key Laboratory of Luminescence and Applications, Changchun Institute of Optics, Fine Mechanics and Physics, Chinese Academy of Sciences, Changchun, 130033, China

ARTICLE INFO

Article history:
Received 24 March 2023
Accepted 17 May 2023
Available online 22 May 2023

Keywords:
LPBF-NiTi alloy
Nanolaser processing
Orthogonal experiment
Superhydrophobic
Corrosion resistance

ABSTRACT

Nickel-titanium (NiTi) is the most ordinarily used shape memory alloy (SMAs), which has important implications in aerospace, medical devices and so on. However, NiTi parts were limited in their application scope and ability due to the difficulty of processing. Until the appearance of laser powder bed fusion (LPBF) technology, it overcame NiTi alloy preparation's multiple challenges and became the preferred method to fabricate NiTi alloy. Nevertheless, the NiTi parts fabricated by LPBF that have a great shortage still exist in corrosion resistance. Therefore, in this paper, a series of micro-nano structures with different characteristics were constructed in LPBF-NiTi by orthogonal experiment for the first time, which wants to explore the degree of influence of various parameters on the wettability of samples. After variance analysis, the nanolaser processing parameters which are most suitable for constructing lotus leaf structures on NiTi alloy surfaces are obtained. The surface morphology and composition were studied by SEM, XRD, EDS, and XPS, respectively. Finally, the corrosion resistance of samples was tested by electrochemical analysis. The results show that the laser power during processing has the greatest influence on the surface morphology of LPBF-NiTi alloy. And the wettability is affected by surface morphology and −CF/-CF2 adsorption. Furthermore, we compared the corrosion resistance of the superhydrophobic samples which was obtained based on the variance analysis with that of the substrate in 3.5 wt% NaCl solution. The result shows that the corrosion resistance and corrosion stability of superhydrophobic samples are brilliantly increased compared with the substrate.

* Corresponding author.
** Corresponding author.
E-mail addresses: zzxu20@jlu.edu.cn (Z. Xu), zlyu@jlu.edu.cn (Z. Yu).

https://doi.org/10.1016/j.jmrt.2023.05.162

1. Introduction

Laser powder bed fusion of NiTi (LPBF-NiTi) has excellent features, including direct moulding of complex parts and low impurity levels (e.g., oxygen, carbon) [1], which aroused wide interest in aerospace and medical devices [2]. However, LPBF-NiTi alloy is limited in its application in engineering fields due to its insufficient corrosion resistance [3,4]. Recently, fabricating superhydrophobic structure on the metallic surface has initiated extensive research interest because the air layer on the superhydrophobic surface can adequately inhibit the direct contact between the metal substrate and the corrosive interface, reducing the corrosion rate and achieving the role of corrosion protection accordingly [5–11].

Almost all ways for preparing the superhydrophobic surfaces of metals are based on two procedures. Firstly, fabricate the micro-nano structure on the substrate surface and then modify it for low free energy surface by fluorination treatment [12–15] or heating treatment [16,17]. Last few years, many mature methods, such as laser ablation, anodizing, chemical conversion [18], electroplating [19], or chemical plating [20], have been applied to the prepared micro-nano structure on metals surface. However, some methods are not suitable for LPBF-NiTi alloy due to which has disadvantages such as long preparation periods, high costs and poor reproducibility. Nanolaser processing is a reliable and accurate method of laser ablation. Therefore, the method has become a promising choice for the generation of micro-/nano-structure at the metal surface [21–23].

In the past two decades, the effect of nanolaser processing on the surface superhydrophobic or corrosion resistance of metallic materials has been widely studied. Ta et al. [24] prepared surfaces on 304S15 stainless steel by nanolaser processing with different wettability and proved that the laser power was positively correlated with the contact angles (CAs) due to the increase in roughness of the samples by the increase of laser power. Ludmila et al. [25] reported the superhydrophobic surfaces fabricated with nanolaser processing on the AMG aluminium-magnesium alloy. And it was found that the increase in scanning times (less than ten times) had an auxo-action on the enhancement of corrosion resistance about the AMG aluminium-magnesium alloy. Chen et al. [26] considered the scanning speed was negatively correlated with the CAs, while the sliding angle (SA) was positively correlated. And they believed that the larger the CAs, the higher the corrosion resistance. All these results showed that the superhydrophobicity and corrosion resistance of metals could be affected directly through nanolaser processing parameters, we can further improve the wettability and corrosion resistance of metal surfaces by optimizing the processing parameters. However, so far, to our knowledge, existing studies have been conducted with variations of a single parameter, while the relationship between the simultaneous change of multiple parameters and the metal surface superhydrophobicity has been no reported. Therefore, it is necessary to systematically evaluate the influence of different processing parameters on sample wettability during laser processing.

In this paper, nanolaser processing was used to prepare four typical micro-nano structure on LPBF-NiTi alloy surfaces, and some samples with a superhydrophobic surface was obtained after ultrasonic fluorination. We used the design of orthogonal experiments for the first time and the variance analysis to systematically evaluate the level of influence of all the parameters on the surface wettability of processed samples in the process of laser processing. In addition, the mechanism of sample wettability transformation was studied and through electrochemical experiments evaluated systematically the corrosion resistance of the sample which was prepared from optimized parameters in 3.5 wt% NaCl solution.

2. Methods

2.1. Materials

In this experiment, pre-alloyed NiTi powder (55.8 wt% Ni) with a particle size range of 15–45 μm, was established by electrode induction melting gas atomization (EIGA, Shenzhen Minatech Co Ltd, China). Samples (10 mm × 10 mm × 5 mm) were prepared by selective laser melting (SLM) equipment (BLT S210, China) with the best parameters from previous studies [27]. The sample was sanded to 2000# with sandpaper before processing and then polished with alumina powder to obtain a mirror-finish surface without scratches.

2.2. Sample fabrication

The surface of the polished sample was processed by a nanolaser system (AVIA 355-14) production of the United States to prepare a rough surface. The system wavelength was 354.7 nm, the pulse frequency was 40 ns, and the 1/e2 laser diameter was 3.5 mm. Table 1 presents the machining parameters designed in the orthogonal experiments, which used different nanolaser power (P, 8–12 W), nanolaser scaning interval (H, 30–50 μm), nanolaser scaning speed (V, 300–700 mm/s) and number of scans (N, 1–5 frequency). The meticulous processing strategy is illustrated in Fig. 1. Table 2 provide the table of the orthogonal experimental for the L9 (34) orthogonal array with 4-column, 9-row.

2.3. Characterization and measurement of samples

The surface of samples was observed by scanning electron microscope (SEM, ZEISS EV018, Germany) before and after fluoridation treatment, and the elemental ingredients of the samples were research analyzed by an energy dispersive spectrometer (EDS, Oxford, UK).

Three-dimensional morphology of processed samples by nanolaser was obtained via white light interference. The CA of the sample was analyzed by the contact angle measuring

Table 1 – Experimental levels of machining parameters.

Symbol	Control parameters	Level 1	Level 2	Level 3
P	Laser power (W)	8	10	12
V	Scan Speed (mm/s)	300	500	700
H	Scan interval (μm)	30	40	50
N	Number of scans (Fre)	1	3	5

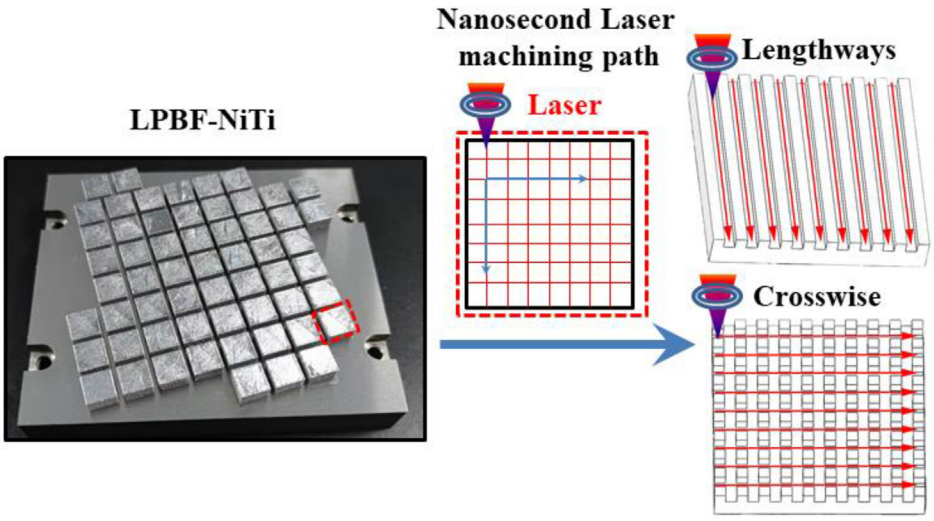

Fig. 1 – Schematic diagram of nanolaser processing path.

instrument (SINDIN SDC-350, China), and the final result was obtained by averaging the testing values of 3 repeated measurements (The size of a single droplet is three μL). The chemical bonding components of the samples were analyzed by X-ray photoelectron spectroscopy (XPS, Thermo ESCALAB250, US), and the surface phase composition was examined by X-ray diffractometer (XRD, SHIMADZU XRD-7000, Japan).

The corrosion behaviour of different samples was tested via the electrochemical workstation in 3.5 wt% NaCl solution (25 °C ± 0.5 °C). The three-electrode system was utilized for corrosion tests, in which the samples with a test area of 1 cm^2 as a working electrode, a block of flaky platinum served as the counter electrode, and a saturated calomel electrode was used as the reference electrode. EIS tests were acquired at open-circuit potential (OCP) for 10 mV disturbing potentials with a frequency range of 0.01 Hz–100 kHz. The polarization curve studies were carried out on a sweep rate of 0.001 V/s and potentials of -1V–1V vs SCE. Corrosion potential (E_{corr}) and corrosion current density (I_{corr}) were obtained by Tafel extrapolation.

The immersion tests were implemented in 3.5 wt% NaCl solution (25 ± 0.5 °C). During the test, the change in corrosion properties of the samples was detected via EIS measurements.

Table 2 – L_9(34) The table of orthogonal Experimental.

Sample	Laser power(P) W	Scan Speed(V) mm/s	Scan interval(H) μm	Number of scans(N) Fre
1	1(8)	1(300)	1(30)	1(1)
2	1	2(500)	2(40)	2(3)
3	1	3(700)	3(50)	3(5)
4	2(10)	1	2	3
5	2	2	3	1
6	2	3	1	2
7	3(12)	1	3	2
8	3	2	1	3
9	3	3	2	1

The nanolaser processed samples were ultrasonically treated [28] during one 1 wt% ethanol (C2H5OH) solution of 1H, 1H, 2H, 2H-Perfluorodecyltriethoxysilane (C16F17H19O3Si).

3. Results and discussion

3.1. *Surface microstructure characterization*

The microstructure of samples in the orthogonal experiment is illustrated in Fig. S1. In general, the samples after laser processing presented four typical characteristics, as shown in Fig. 2. Nanosecond laser cannot effectively ablate the surface of these samples (Samples 1, 2, 3 and 5) when the laser power is insufficient, but only a small protrusion will be made on the surface of the sample (Fig. 2a). When the nanolaser scanning frequency was insufficient, the mastoid structure of sufficient height (Fig. 2b) cannot be formed on the samples (Sample 6 and 9) surface even if the laser power was sufficient. The surface of samples (Sample 4 and 7) would appear neat and beautiful mastoid structures (Fig. 2c) when the laser power was sufficient to ablate the sample surface and is compatible with the scanning frequency, speed and spacing. Due to the laser in the processing of the substrate, the laser spot inside and outside the energy produced was very different, so the laser irradiation melted material would splash outward, these materials after cooling accumulate in the periphery, with the increase of scanning times gradually form the mastoid structure. On the contrary, when the laser power was too large, the structure of the sample (Sample 8) surface would be destroyed, and the ablation phenomenon would be formed (Fig. 2d).

At the same time, in order to represent different structures more directly, we obtained the 3D image of LPBF-NiTi alloy, which is processed by the nanolaser, through the white light interference experiment, as shown in Fig. 3. Through the 3D

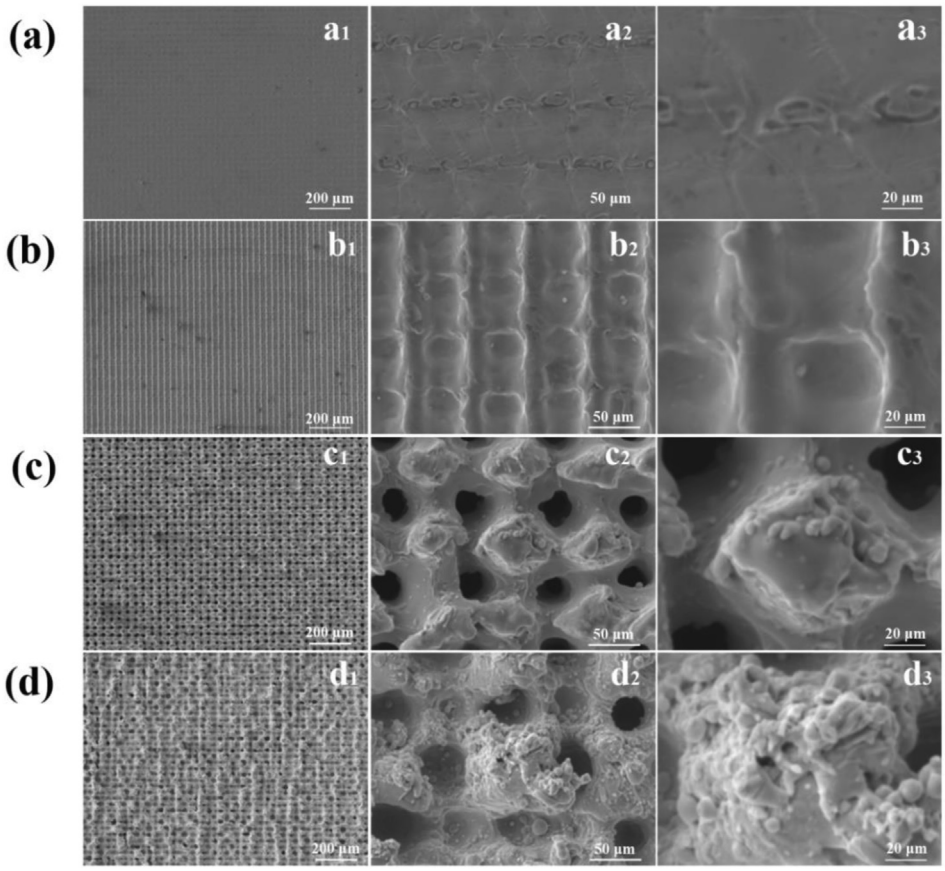

Fig. 2 – SEM image of LPBF-NiTi alloy with nanolaser processing, (a) Sample 1, (b) Sample 6, (c) Sample 4, (d) Sample 8.

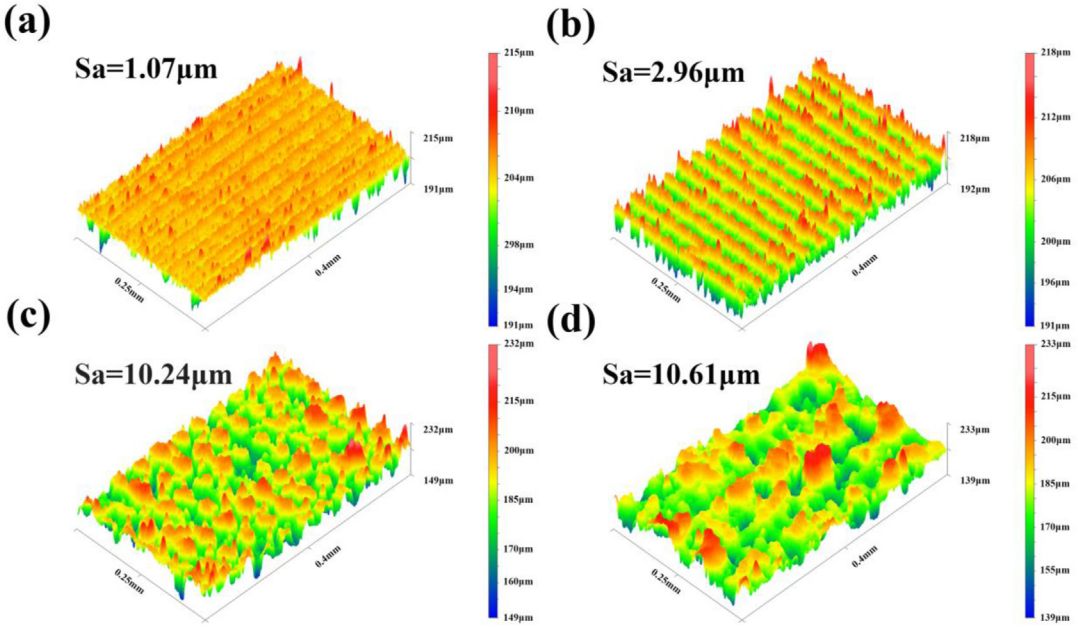

Fig. 3 – Three-dimensional topography of samples by nanolaser processing, (a) Sample 1, (b) Sample 6, (c) Sample 4, (d) Sample 8.

images of samples can be observed when the laser energy was insufficient (which occurs when the laser power was too low, or the scanning frequency was insufficient, or the scanning speed was too fast), the prepared surface structure was small in height and depth, resulting in failure to form the distinct mastoid structure (Fig. 3a and b) on the surface of samples. The surface roughness (Sa) of these two surfaces was relatively small, which is 1.07 μm and 2.96 μm, respectively. When the laser energy was appropriate, the Sa of the sample (Fig. 3c) increased rapidly due to the formation of mastoid structures with good size. However, when the laser energy was too large, the surface of the samples would appear to be an ablation phenomenon (Fig. 3d). The partial adjacent mastoid structures of the sample were melted and joined together, so the Sa did not increase significantly after nanolaser processing. The results indicate that a regular and well-sized mastoid structure of samples needs appropriate processing parameters, and the surface roughness of the sample will increase obviously when the mastoid structure appears on the surface of the sample.

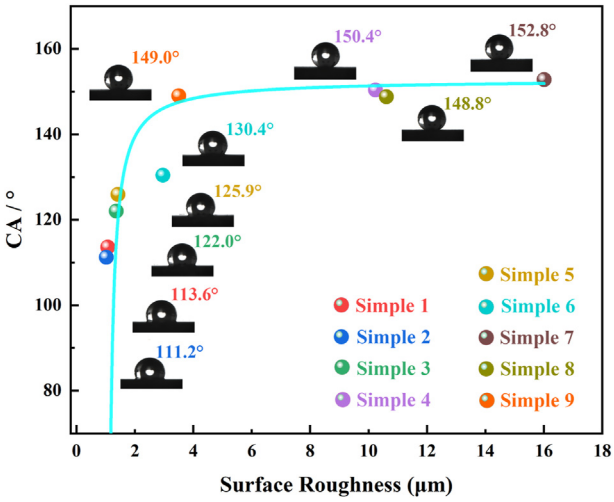

Fig. 4 – Variation of CAs with sample's surface roughness.

3.2. *Contact angle analysis*

Hydrophilic metal surfaces developed superhydrophilic properties (CA of 0°) with increased roughness. NiTi alloy has high surface energy and good hydrophilicity. Therefore, increased roughness of the sample surface increased after nanolaser processing and showed super hydrophilic (CAs is 0° as shown in Fig. S2). Ultrasonic fluorination can significantly reduce the surface energy of materials and thus enhance the CAs of its progressive change from the hydrophilic to the hydrophobic state. However, after fluoridation, the CAs of samples with different roughness increased to different degrees. The roughness of each sample and the respective CAs are displayed in Table 3.

In order to research the connection between the surface roughness and the CAs of the fluorinated samples more directly, the patterns change of CAs with the surface roughness of the samples after fluorination is revealed in Fig. 4. The results showed that with the increase of the sample surface roughness, the CA increased quickly. In particular, Sample 4 and Sample 7 were superhydrophobic, with CA values of 150.4° and 152.8°, respectively, which correspond to their high roughness (10.24 μm and 16.01 μm). However, when the surface of the samples (Sample 8) was overfired, even with the high roughness of these samples, the fluorinated samples were not superhydrophobic, which is consistent with previous studies [29,30]. Therefore, in order to realize the superhydrophobicity of the metal surface, the surface structure (mastoid structure) of the sample surface needs to be intact, i.e., appropriate process parameters. Interestingly, both sample 4 (150.4°) and sample 7 (152.8°) have larger CA than at 150.3° (the CA of LPBF-NiTi superhydrophobic surface prepared in previous studies [31]), which fully demonstrates the necessity of parameter optimization."

Table 3 – L_9(34) orthogonal array, control parameters, and observed values.

Sample	Surface Roughness(Sa) μm	CA
1	1.071	113.6
2	1.022	111.2
3	1.363	122.0
4	10.24	150.4
5	1.425	125.9
6	2.962	130.4
7	16.01	152.8
8	10.61	148.8
9	3.508	149.0

3.3. *Chemical composition*

XRD and EDS were used to analyze the component changes on the surface of these samples before and after fluorination, revealing the reasons for the transition in wettability of the sample surface.

Fig. 5 demonstrated the XRD patterns of LPBF-NiTi alloy, which was nanolaser processed and fluoridation treatment. The B2 phase and B19' phase are the main phase components of the LPBF-NiTi alloy. The results show that a new TiO2 phase appears after all samples have been nanolaser processed. This is due to the combination of O2- in the air with Ti4+ on the surface of the substrate when the sample surface is irradiated by the laser during the nanolaser processing. At the same time, it was found that the intensity of the B19 phase was reduced plenty (all samples), and the B2 phase's intensity was increased considerably (all samples) after nanolaser processing. These changes may be due to high laser beam energy restraining the formation of the B19' phase and therefore stabilizing the B2 phase during the nanolaser processing. The XRD pattern of the samples did not change basically (Fig. 5a and c) before and after fluoridation treatment. Only the peak intensity of the B2 phase was slightly increased (Fig. 5d) at ~63° or reduced (Fig. 5b) at ~42°, which testified that the fluoridation treatment had less effect on the phase structure of samples [32]. The results show that the transformation of wettability is independent of the phase structure.

Fig. S3 and Fig. 6 depicted the EDS result of LPBF-NiTi before and after fluoridation which was processed by nanolaser. The

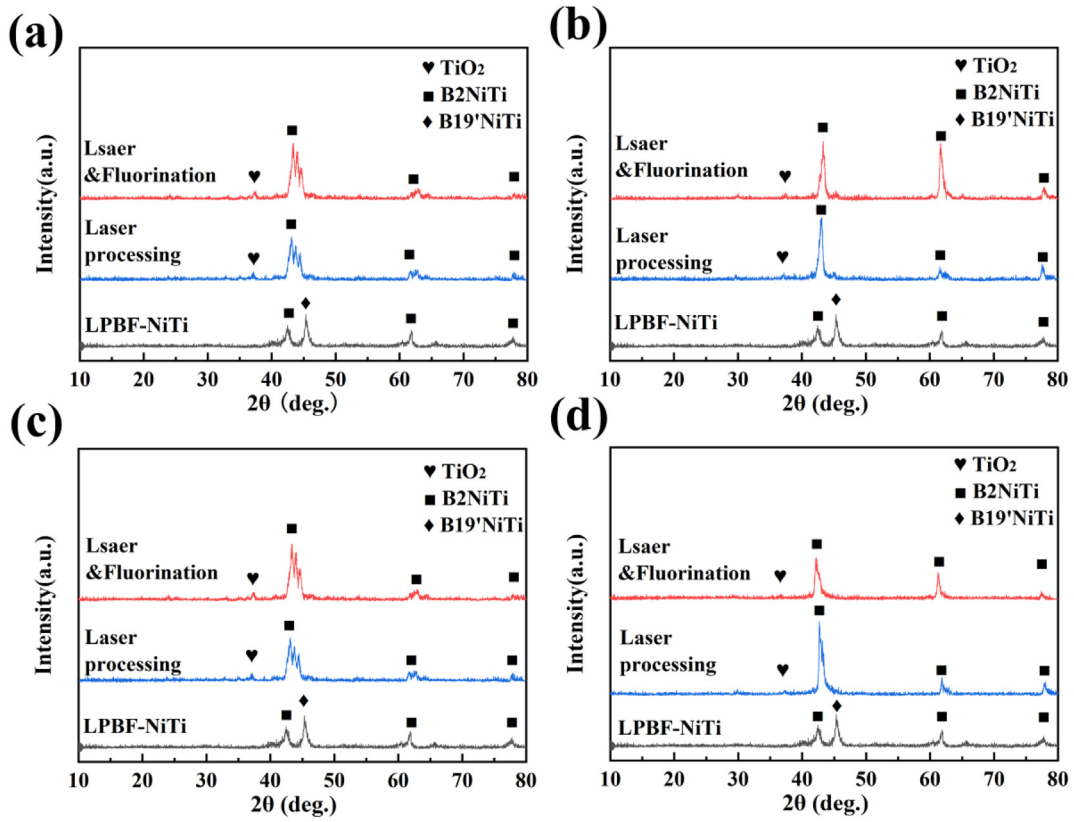

Fig. 5 – XRD patterns of samples nanolaser processing and after fluorination (a) Sample 1, (b) Sample 6, (c) Sample 4, (d) Sample 8.

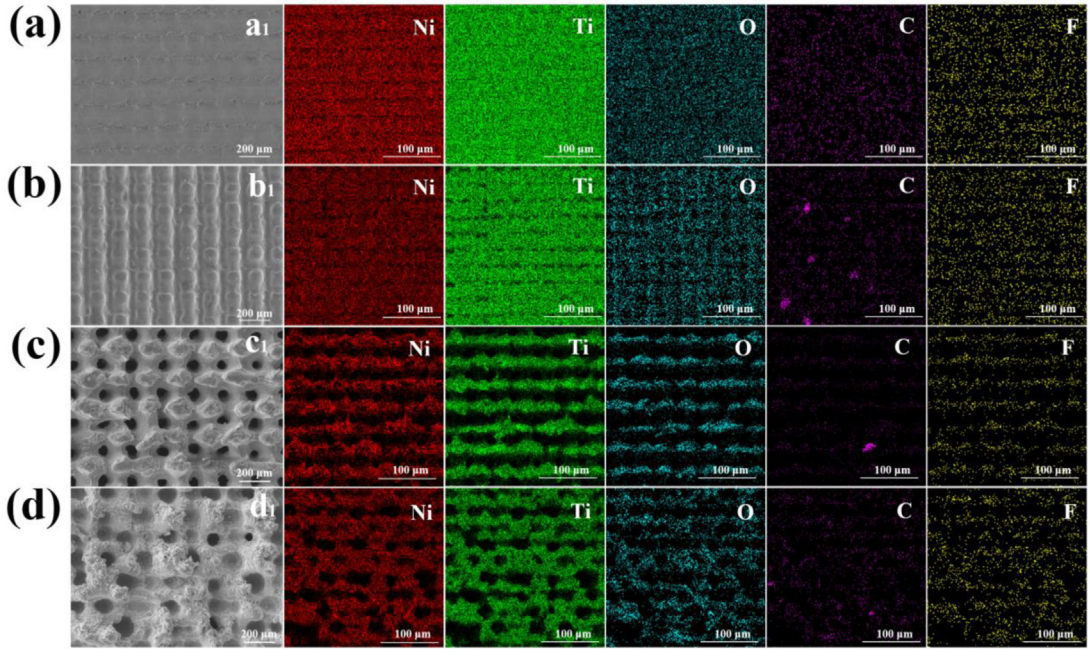

Fig. 6 – Distribution of elements on the surface of the sample after fluoridation treatment, (a) Sample 1, (b) Sample 6, (c) Sample 4, (d) Sample 8.

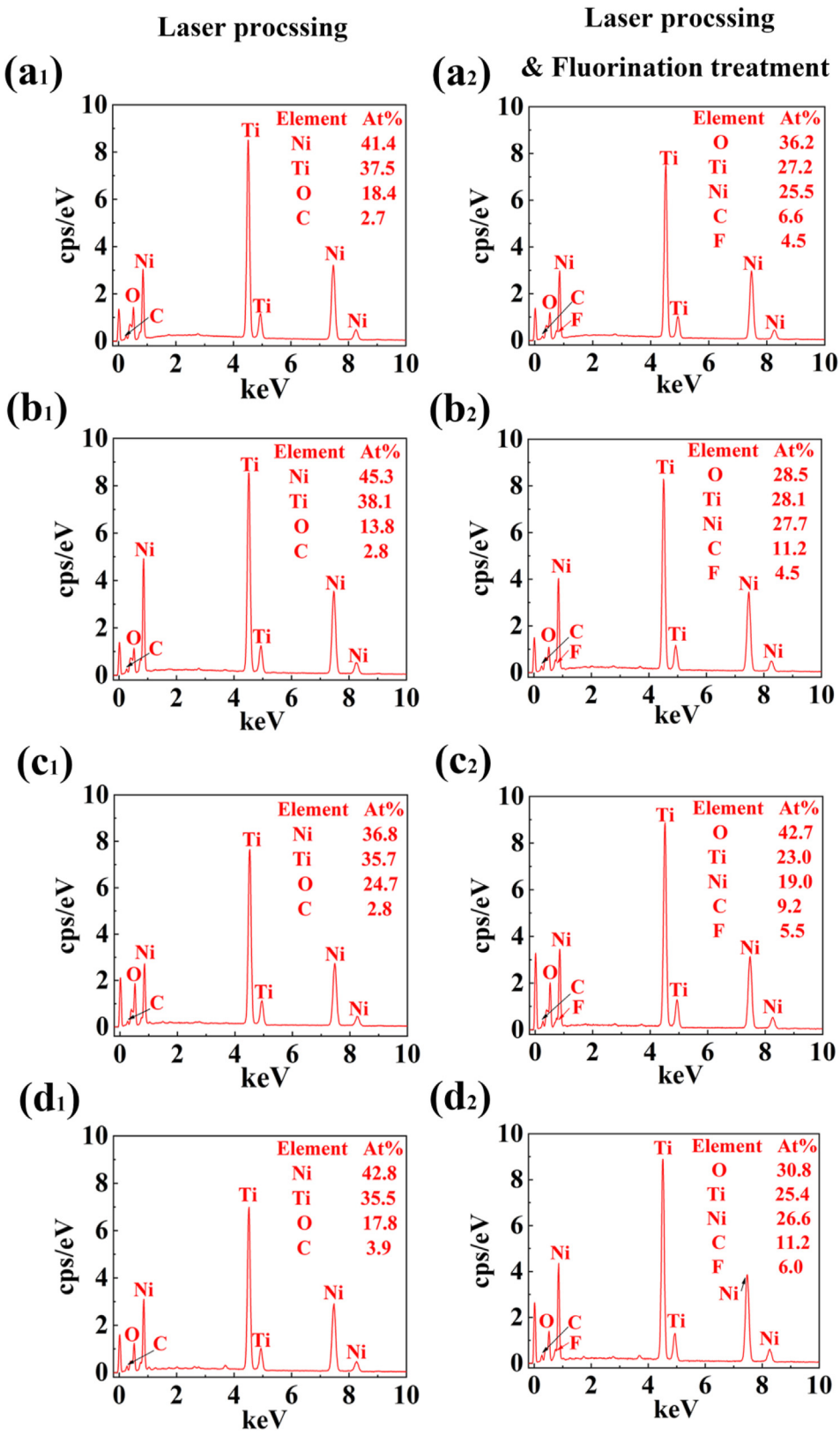

Fig. 7 – Surface element content diagram of samples before and after fluoridation (a_1, a_2) Sample 1, (b_1, b_2) Sample 6, (c_1, c_2) Sample 4, (d_1, d_2) Sample 8.

results of the element distribution map showed that Ni, Ti and O elements were uniformly distributed on the surface of the mastoid structure before and after fluoridation treatment. Moreover, after fluoridation treatment, the F element appeared on the sample surface and enriched the mastoid structure (Fig. 6c). The presence of the F element proved the fluoridation treatment to be successful, and the mastoid structure could absorb more F elements.

In order to determine the specific change in element content before and after fluoridation, the EDS spectrum results of samples were compared, as shown in Fig. 7. After fluoridation, the content of C, O and F elements on the surface of samples increased significantly, while the contents of Ni element or Ti elements decreased significantly, which was mainly due to introduction of C, F and O in the fluorination process, which covered the substrate on the surface. Therefore, it is considered that the change in element composition after fluoridation is an important factor affecting the CA of samples, and the change in elements C and F may be the main factor.

3.4. *Variance analysis*

The different morphology of the same substrate surface is obviously related to the nanolaser processing parameters (P, h, V, N). Next, we used analysis of variance (ANOVA) to study the influence degree of different nanolaser processing parameters on the surface roughness.

It (Table 4) provides the sensitive factors that influence surface CA changes in nanolaser processing. The results of variance analysis showed that the influence degree of nanolaser power on the CAs of samples was much higher than the influence of V, H and N on the CAs, which reached 34.6. In addition, It was predicted that when the processing parameters of nanolaser are P = 12 W, V = 300 mm/s, N = 5, and H = 40 μm, respectively (named B–NiTi), the nanolaser processed samples would have the maximum CAs after ultrasonic fluorination. The research reveals that the nanolaser power had the greatest influence on the surface morphology of NiTi during nanolaser processing when four parameters changed at the same time, but the influence of V, H and N was equally important. The quality of processing parameters will directly affect the surface roughness of the samples and indirectly affect the CAs of samples after fluorination.

The characteristics of the optimal parameter sample (B–NiTi) obtained by orthogonal experiment are shown in Fig. 8. It could be seen that the surface morphology of B–NiTi had a neat and beautiful mastoid structure (Fig. 8a) with micro-nanostructure sputtered material on the papilla structure (Fig. 8b). The surface roughness (Fig. 8c) obtained by white light interference also accorded with the above analysis, and the content of C element and F element (Fig. 8d) was highest compared other samples after fluorination.

Table 4 – Range analysis of surface roughness.

Range	P	V	H	N
K1	346.8	416.8	392.8	388.4
K2	406.7	385.9	410.5	394.4
K3	450.5	401.3	400.7	421.2
k1	115.6	138.9	130.9	129.5
k2	135.7	128.6	136.3	131.5
k3	150.2	133.8	133.6	140.4
R	34.6	10.3	5.9	10.9

In order to explore the transformation mechanism of the surface wetting state of the sample, XPS was used to identify the evolution of functional groups on B–NiTi. Fig. 9 exhibition the XPS survey of B–NiTi before fluorination treatment, and Fig. 10 gives the high-resolution spectra of B–NiTi after fluorination (All high-resolution spectra are processed by XPS Peaks software). It can be observed that the Ni and Ti contents on the surface of the B–NiTi before and after fluorination were lower, but the difference was that the Ni content was more abundant than the Ti content after fluorination. This may be attributable to the fact that after laser processing, the surface of B–NiTi adsorbed more C compounds in the air or 1%wt ethanol solution of $C_{16}F_{17}G_{19}O_3Si$, which covered the Ni and Ti of the B–NiTi, while the Ni content was higher after fluorination due to the generation of NiF_2. In addition, after fluorination treatment, the B–NiTi's XPS spectra showed new peaks appeared, which include F 1s and Si 2p; the content of F 1s was 57.1% among them. It proved the fluorination treatment was carried out successfully.

To further investigate the specific chemical components of the B–NiTi, all peaks were fitted (derived via XPSpeak). Fig. 9b shows that the C 1s high-resolution spectrum had three main peaks: 284.6 eV, 286.3 eV, 287.9 eV, which were attributed to C–C/C–H, C–O–C, and O–C=O [33], respectively, who only C–C/C–H was a non-polar group. The C 1s high-resolution spectra of B–NiTi after fluorination (Fig. 10b) show that two new peaks of C 1s were located at 290.5 eV (-CF_2 non-polar) and 292.6 eV (-CF non-polar) [34], and they accounted for a very large proportion, while the intensity of O–C=O (polar) peak was significantly reduced. The high-resolution spectra of O1s before and after fluorination treatment (Figs. 9c and 10c) were not significantly different and consisted mainly of three peaks, 530.1 eV, 531.4 eV, 532.6 eV, which were known to come from C–O, Ti–O, –OH groups. Similarly, the high-resolution spectrum of Ti 2p (Figs. 9e and 10e) also did not change significantly, consisting of three peaks, 458.6 eV, 464.3 eV, 460.1 eV belonging to Ti 2p3, Ti 2p3 companion peak, and Ti 2p [35,36], respectively, which were mainly caused by the generation of TiO_2 after laser processing and TiF_3 after fluorination treatment [34,37]. The high-resolution spectra of Ni 2p (Fig. 9d) before the fluorination treatment was mainly divided into three peaks: 855.7 eV, 853.2 eV, 870.8 eV, which were caused by Ni in the oxide. After the fluorination treatment, only two peaks were composed, which resulted from the generation of Ni in NiF_2 (Fig. 10d) [38,39]. Moreover, the high-resolution spectra of F 1s had one main peak: 684.5 eV and a tiny peak: 688.5 eV. This main peak was mainly caused by NiF_2, TiF_3, –CF, $-CF_2$, and the content of CF and $-CF_2$ was well above that of NiF_2 and TiF_3. Another small peak was the formation of $TiO_{2-x}F_x$, which was produced by the combination of element F with TiO_2 on the surface of B–NiTi due to the fluorination process. Fig. 10g shows that the Si 2p high-resolution spectrum had three main peaks: 99.6 eV, 102.5 eV, 103.7 eV, which were attributed to Si–Si, Si–N, and Si–O [40], that were mainly produced by the surface residues of $C_{16}F_{17}H_{19}O_3Si$. Figs. 9f and 10g, respectively, show the content

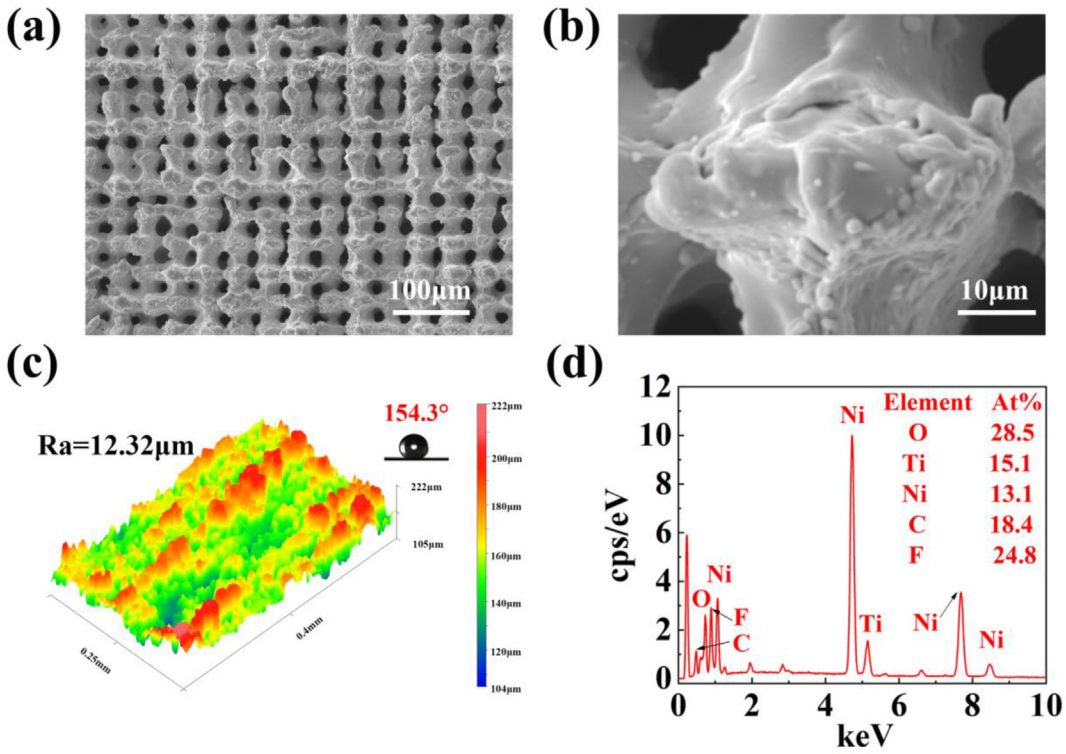

Fig. 8 – The characteristics of B–NiTi (a, b) SEM image, (c) Three-dimensional topography, (d) Surface element content diagram after fluoridation treatment.

of C1s peak polar bond and non-polar bond on the B–NiTi surface before and after fluoridation treatment. It can be found that the content ratio of CF_2 and CF (non-polar) increased significantly after fluoridation treatment, which effectively reduced the surface energy of the sample.

Therefore, the adsorption of non-polar groups is the crucial factor in changing the CA of the B–NiTi, and only a small part of TiF_3, NiF_2, was generated, which is not the main influencing factor. Due to the formation of many non-polar functional groups (mainly the –CF and $-CF_2$) on the surface of the B–NiTi during fluorination, the surface energy of the B–NiTi will be significantly reduced, thus transforming the B–NiTi from superhydrophilic to superhydrophobic.

3.5. *Electrochemical corrosion behaviors*

For the purpose of studying the electrochemical behaviour of superhydrophobic surfaces, electrochemical experiments were carried out on LPBF-NiTi and fluorinated B–NiTi. The results of the experiments are shown in Fig. 11, and the specific values are given in Table 5. The E_{corr} value shows the degree of activity of the sample. The larger *the* E_{corr} value, the less active the sample surface and the less likely to be corroded [41,42]. On the contrary, the smaller the I_{corr} of materials, the larger its electrical resistance, and the even lower the rate of being corroded [43]. For fluorinated B–NiTi, the E_{corr} showed a positive shift phenomenon, from −0.43 V to −0.21 V, and I_{corr} was also reduced by about 10 times, from $(4.42 \pm 0.5) \times 10^{-7}$ A/cm^2 to $(2.27 \pm 0.5) \times 10^{-10}$A/cm^2.

The Nyquist plot for LPBF-NiTi, Pre-NiTi and fluorinated B–NiTi is shown in Fig. 11b and c. The size of the radius of the capacitor circuit usually indicates the corrosion resistance of the tested materials, and when it is larger, the sample is more resistant to corrosion [44,45]. It is obvious that the radius of the capacitance ring of fluorinated B–NiTi was larger than that of LPBF-NiTi alloy. The fluorinated B–NiTi exhibited higher |Z| than the LPBF-NiTi alloy at the low frequency of the Bode |Z| value map (Fig. 11d). This also reveals the excellent corrosion resistance of fluorinated B–NiTi [45]. The Bode phase plots of the fluorinated B–NiTi (Fig. 11e) show that there was a time constant in the low-frequency region and one in the high-frequency region, respectively. Moreover, fluorinated B–NiTi had higher and wider phase angle values than LPBF-NiTi in the middle-frequency region.

The corresponding equivalent circuit (EC) is shown in Fig. 11f to reveal the mechanism of corrosion resistance LPBF-NiTi alloy and B–NiTi. The equivalent circuit used for LPBF-NiTi alloy had one time constant, and that of fluorinated B–NiTi had two. In the EC, R_s represents the solution resistance, the charge transfer resistance is noted as R_{ct}, and CPE_1 and CPE_2 are perceived as the constant phase element, which is used for replacing pure capacitance. R_f represents the resistance of the TiO_2 layer after sample oxidation.

The values in the columns of Table 6 are the fitted values for samples in EC. The Y_0 of fluorinated B–NiTi is reduced by a factor of about 100 compared to the LPBF-NiTi alloy, which suggests that the sample surface is corroded in a smaller area [45]. The R_{ct} value of fluorinated B–NiTi increases

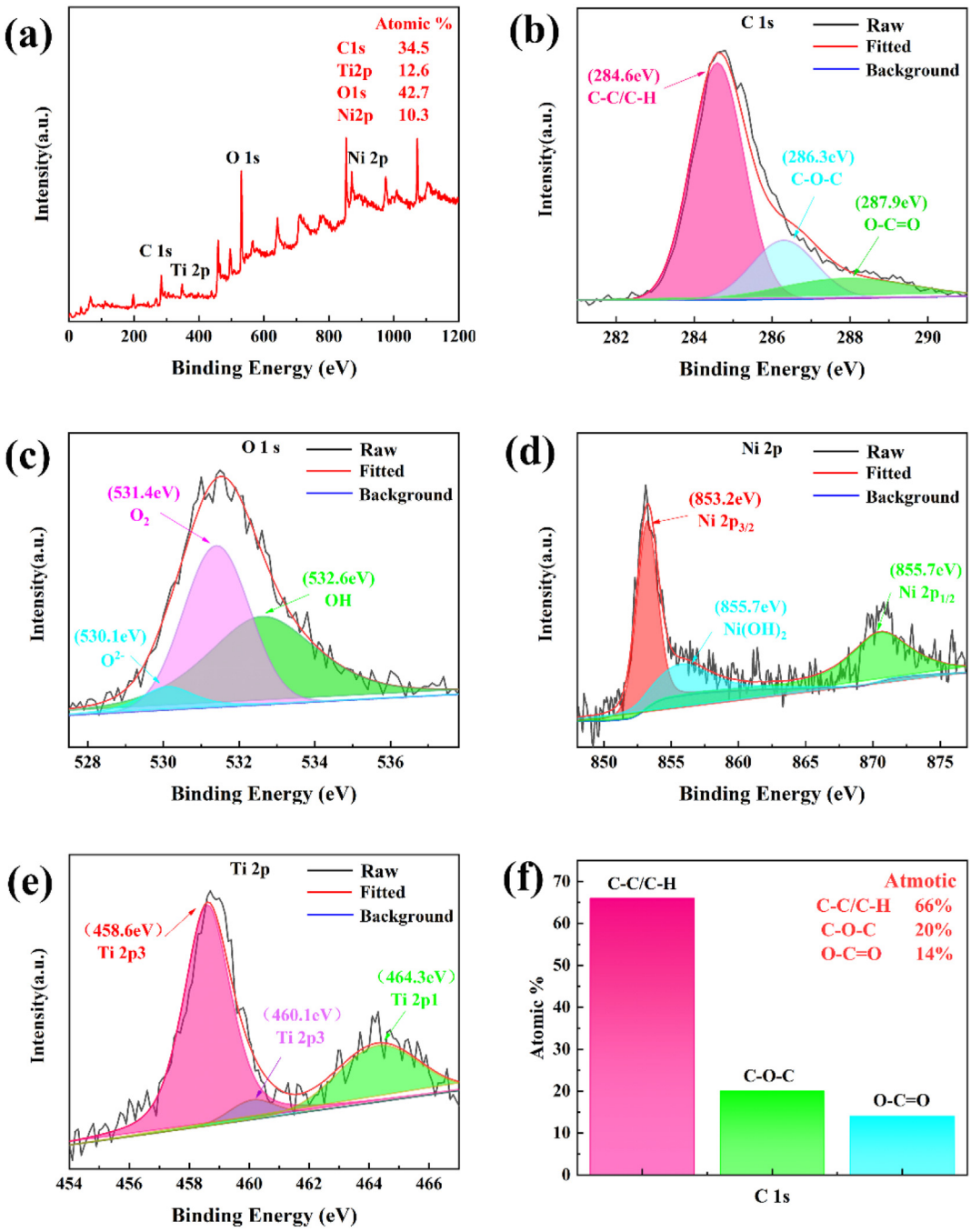

Fig. 9 – XPS spectra of B–NiTi surfaces before fluoridation, (a) Survey spectra, (b) High-resolution C 1s, (c) High-resolution O 1s, (d) High-resolution Ni 2p, (e) High-resolution Ti 2p, (f) Percentage ratio of C group.

significantly, and usually, the larger the R_{ct}, the better the corrosion resistance of the sample [46]. This is the same outcome as the polarization curve.

3.6. *Immersion tests*

In order to further study the stability of B–NiTi after fluoride treatment, it was immersed in 3.5 wt% NaCl solution for a 15-day immersion experiment. Fig. 12 Shows EIS curves of fluorinated B–NiTi soaked in 3.5 wt% NaCl solution for a different time and corresponding fitting results. The Nyquist plot for fluorinated B–NiTi showed that the size of the capacitor circuit's radius changed little, proving that the corrosion resistance stability of the fluorinated B–NiTi is preferable. In the Bode |Z| value plot (Fig. 12b), |Z| values showed less fluctuation in the low-frequency region during the immersion, which indicated that fluorinated B–NiTi still maintained good corrosion resistance after 360 h immersion. The same result can be seen in the variation of the phase angle graph (Fig. 12c). The results show that the prepared

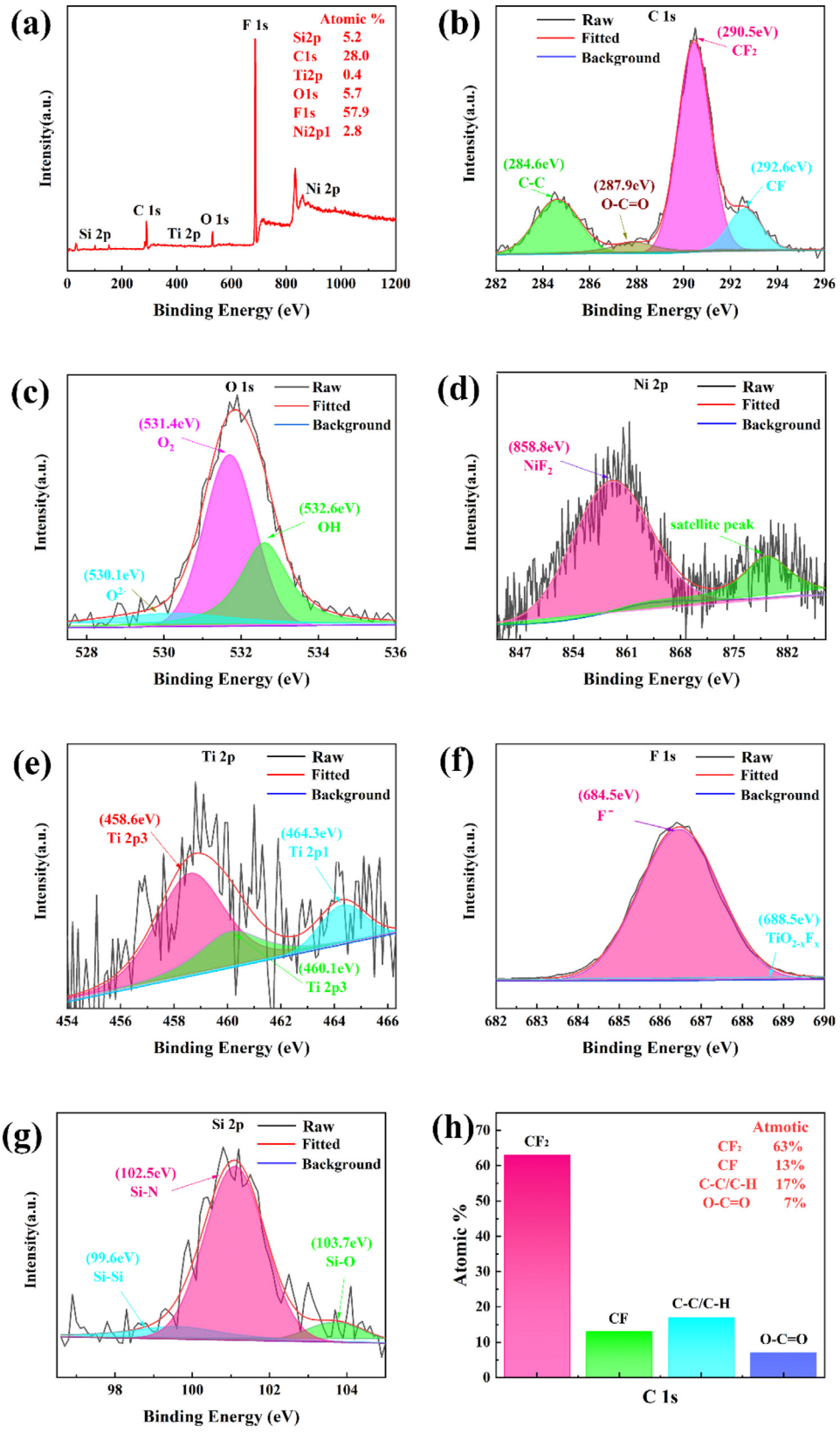

Fig. 10 – XPS spectra of B–NiTi surfaces after fluoridation (a) Survey spectra, (b) High-resolution C 1s, (c) High-resolution O 1s, (d) High-resolution Ni 2p, (e) High-resolution Ti 2p, (f) High-resolution F 1s (g) High-resolution Si 2p (h) Percentage ratio of C group.

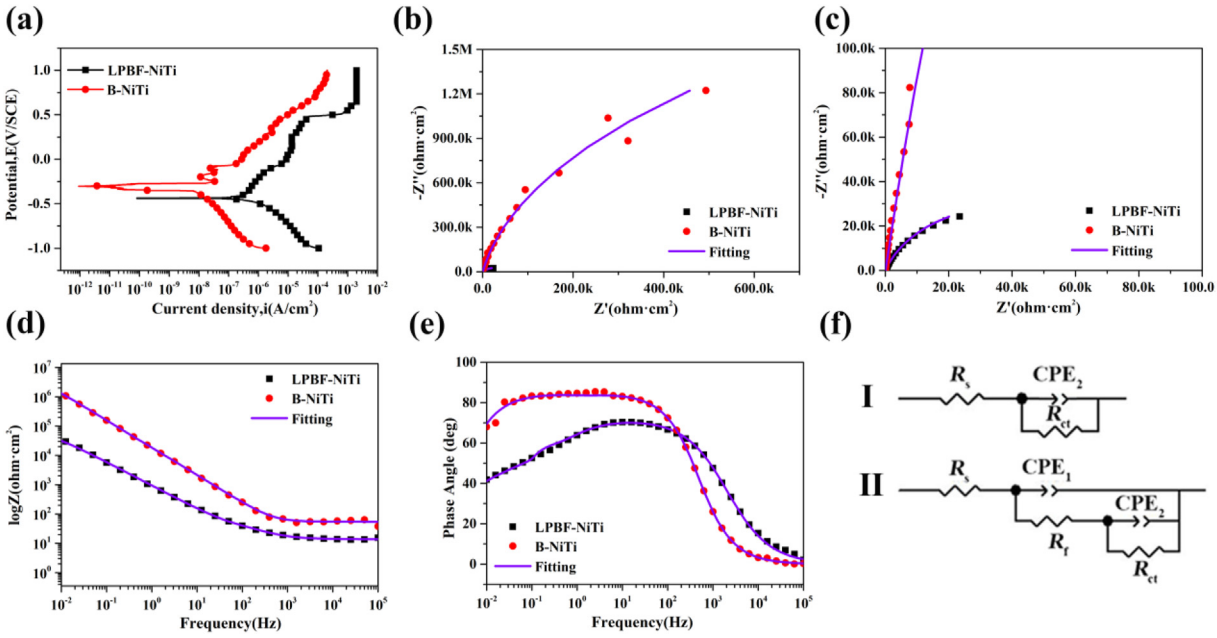

Fig. 11 – Polarization curves and EIS results of LPBF-NiTi alloy and fluorinated B–NiTi, (a) Polarization curves, (b) Nyquist plots, (c) An enlarged view of the Nyquist diagram, (d) Bode |Z| value plots, (e) Phase angle plots, (f) equivalent circuit of LPBF-NiTi (I) and B–NiTi (II).

Table 5 – Parameters obtained from polarization curves of LPBF-NiTi, Pre-NiTi and fluorinated B–NiTi.

Sample	E_{corr} (V)	I_{corr} (A/cm^2)	R_p (KΩ·cm^2)
LPBF-NiTi	−0.43 ± 0.04	(4.42 ± 0.5) × 10^{-7}	88.5
B–NiTi	−0.26 ± 0.03	(2.27 ± 0.5) × 10^{-10}	360.2

Table 6 – The fitted values of EIS measurements.

Samples	R_s (Ω·cm^2)	R_f (Ω·cm^2)	CPE_1		R_{ct} (Ω·cm^2)	CPE_2	
			Y_{02} (Ω^{-1}·s^n·cm^{-2})	n_1		Y_{02} (Ω^{-1}·s^{n}cm^{-2})	n_2
LPBF-NiTi	10.61 ± 1.2				(6.21 ± 0.3) × 10^4	(1.53 ± 0.3) × 10^{-4}	0.81 ±0.02
B–NiTi	70.03 ± 3.2	2.34 ± 0.3×10^3	2.51 ± 0.3×10^{-6}	0.80 ± 0.4	(4.43 ± 0.2) × 10^5	(3.92 ± 0.5) × 10^{-6}	0.66 ±0.04

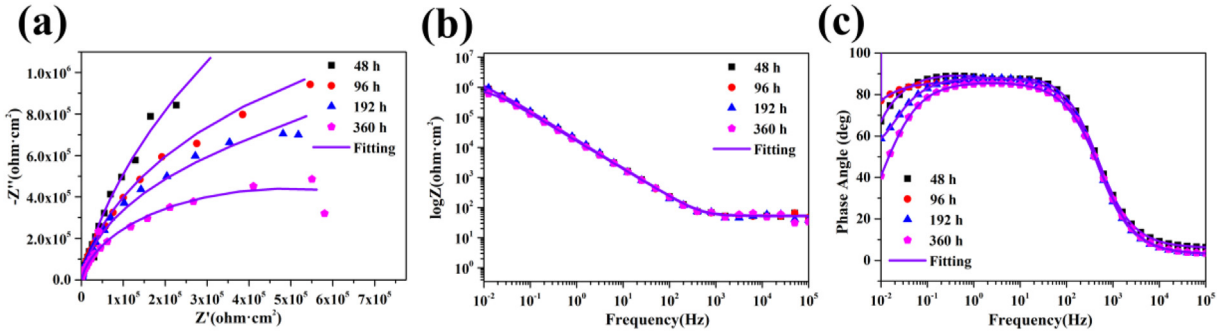

Fig. 12 – EIS curves and the fitted results of B–NiTi immersed in 3.5% NaCl for 360 h (a) Nyquist plots (b) Bode |Z| value plots, (c) Phase angle plots.

B–NiTi have excellent corrosion stability after fluoride treatment.

4. Conclusions

"In this paper, four kinds of micro and nanostructures with different characteristics were prepared on the surface of LPBF-NiTi alloy by a nanolaser through an orthogonal experiment for the first time. The CAs of these fluorinated samples increase with the increase of Sa when the surface is not ablated. The influence of each processing parameter on the wettability of the sample was further studied by variance analysis. It was found that the laser power played a decisive role in the final wettability of the sample during laser processing. In addition, the principle of wettability transformation of samples was studied. The XRD results showed that the CA of the sample surface was not related to the phase composition. The XPS results justify that the –CF⟍-CF2 generated on the surface of the sample after fluorination is a crucial factor affecting its CA. The results of electrochemical experiments as well as immersion experiments in 3.5 wt% NaCl solution showed that the corrosion resistance and corrosion stability of superhydrophobic samples are distinguish increased compared with the substrate. This provides a new means for the application and life extension of LPBF-NiTi alloy in the ocean. In addition, a fast and efficient treatment method for improving the corrosion resistance of metal materials in NaCl solution was obtained."

Declaration of competing interest

The authors declare that they have no known competing financial interests or personal relationships that could have appeared to influence the work reported in this paper.

Acknowledgments

This work was supported by the National Key R&D Program of China, China (No. 2022YFB4601701), the National Natural Science Foundation of China, China (No. 51975246, 52205310), Science and Technology Development Program of Jilin Province, China (20230508045RC), the Natural Science Foundation of Shandong Province, China (No. ZR2021QE263), the Capital construction fund plan within the budget of Jilin Province, China (No. 2023C041-4), the Chongqing Natural Science Foundation, China (No. CSTB2022NSCQ-MSX0225), the Interdisciplinary Research Fund for Doctoral Postgraduates of Jilin University, China (No.101832020DJX052) and the Interdisciplinary Cultivation Project for Young Teachers and Students, China (No. 415010300078).

Appendix A. Supplementary data

Supplementary data to this article can be found online at https://doi.org/10.1016/j.jmrt.2023.05.162.

REFERENCES

[1] Wang X, Yu J, Liu J, Chen L, Yang Q, Wei H, et al. Effect of process parameters on the phase transformation behavior and tensile properties of NiTi shape memory alloys fabricated by selective laser melting. Addit Manuf 2020;36.
[2] Haberland C, Elahinia M, Walker JM, Meier H, Frenzel J. On the development of high quality NiTi shape memory and pseudoelastic parts by additive manufacturing. Smart Mater Struct 2014;23(10).
[3] Zhang QC, Dong JJ, Peng MX, Yang ZW, Wan YZ, Yao FL, et al. Laser-induced wettability gradient surface on NiTi alloy for improved hemocompatibility and flow resistance. Materials Science and Engineering C-Materials for Biological Applications 2020;111.
[4] Wang H, Jurgensen J, Decker P, Hu ZY, Yan K, Gurevich EL, et al. Corrosion behavior of NiTi alloy subjected to femtosecond laser shock peening without protective coating in air environment. Appl Surf Sci 2020;501.
[5] Li H, Yu S, Han X, Zhao Y. A stable hierarchical superhydrophobic coating on pipeline steel surface with self-cleaning, anticorrosion, and anti-scaling properties. Colloids Surf A Physicochem Eng Asp 2016;503:43–52.
[6] Ruiz-Cabello FJM, Ibanez-Ibanez P, Paz-Gomez G, Cabrerizo-Vilchez M, Rodriguez-Valverde MA. Fabrication of superhydrophobic metal surfaces for anti-icing applications. Jove-Journal of Visualized Experiments 2018;138.
[7] Lan X, Zhang B, Wang J, Fan X, Zhang J. Hydrothermally structured superhydrophobic surface with superior anti-corrosion, anti-bacterial and anti-icing behaviors. Colloids Surf A Physicochem Eng Asp 2021;624.
[8] Mohamed ME, Abd-El-Nabey BA. Fabrication of a biological metal-organic framework based superhydrophobic textile fabric for efficient oil/water separation. Sci Rep 2022;12(1):15483.
[9] Toma M, Loget G, Corn RM. Flexible Teflon nanocone array surfaces with tunable superhydrophobicity for self-cleaning and aqueous droplet patterning. ACS Appl Mater Interfaces 2014;6(14):11110–7.
[10] He H, Hua R, Li X, Wang C, Ning X, Sun L. Fabrication of superhydrophobic Ti-6Al-4V surfaces with single-scale micotextures by using two-step laser irradiation and silanization. Materials 2020;13(17).
[11] Wang Z, Song J, Wang T, Wang H, Wang Q. Laser texturing for superwetting titanium alloy and investigation of its erosion resistance. Coatings 2021;11(12).
[12] Zheng HP, Liu L, Meng FD, Cui Y, Li Z, Oguzie EE, et al. Multifunctional superhydrophobic coatings fabricated from basalt scales on a fluorocarbon coating base. J Mater Sci Technol 2021;84:86–96.
[13] Zheng BX, Jiang GD, Wang WJ, Mei XS. Fabrication of superhydrophilic or superhydrophobic self-cleaning metal surfaces using picosecond laser pulses and chemical fluorination. Radiat Eff Defect Solid 2016;171(5–6):461–73.
[14] Li XJ, Yin SH, Huang S, Luo H, Tang QC. Fabrication of superhydrophobic magnesium alloy surface for water-repellent, 9th international symposium on advanced optical manufacturing and testing technologies - subdiffraction-limited plasmonic lithography and innovative manufacturing technology. Chengdu: PEOPLES R CHINA; 2018.
[15] Cai QQ, Xu JK, Lian ZX, Yu ZJ, Yu HD, Li J. Superhydrophobic magnesium alloy surface with corrosion resistance, annual IEEE international conference on manipulation, manufacturing and measurement on the nanoscale (3M-NANO). Xian: PEOPLES R CHINA; 2021. p. 328–31.

[16] Yamamoto R, Kowalski D, Zhu RJ, Wada K, Sato Y, Kitano S, et al. Fabrication of superhydrophobic copper metal nanowire surfaces with high thermal conductivity. Appl Surf Sci 2021;537.
[17] Jie H, Xu QJ, Wei L, Min YL. Etching and heating treatment combined approach for superhydrophobic surface on brass substrates and the consequent corrosion resistance. Corrosion Sci 2016;102:251–8.
[18] Ge-Zhang S, Yang H, Ni H, Mu H, Zhang M. Biomimetic superhydrophobic metal/nonmetal surface manufactured by etching methods: a mini review. Front Bioeng Biotechnol 2022;10:958095.
[19] Zhou JX, Zhao GC, Li JS, Chen J, Zhang SQ, Wang J, et al. Electroplating of non-fluorinated superhydrophobic Ni/WC/WS2 composite coatings with high abrasive resistance. Appl Surf Sci 2019;487:1329–40.
[20] Yuan J, Wang JH, Zhang KL, Hu WB. Fabrication and properties of a superhydrophobic film on an electroless plated magnesium alloy. RSC Adv 2017;7(46):28909–17.
[21] Wang QH, Wang HX, Zhu ZX, Xiang N, Wang ZD, Sun GF. Switchable wettability control of titanium via facile nanosecond laser-based surface texturing. Surface Interfac 2021;24.
[22] Li Z, Xue G, Wu YM, Wang XH, Pan HP. Preparation of superhydrophobic surfaces based on rod-shaped micro-structure induced by nanosecond laser. Crystals 2021;11(11).
[23] Wang YT, Zhao XY, Ke CJ, Yu J, Wang R. Nanosecond laser fabrication of superhydrophobic Ti6Al4V surfaces assisted with different liquids. Colloid and Interface Science Communications 2020;35.
[24] Ta VD, Dunn A, Wasley TJ, Li J, Kay RW, Stringer J, Smith PJ, Esenturk E, Connaughton C, Shephard JD. Laser textured superhydrophobic surfaces and their applications for homogeneous spot deposition. Appl Surf Sci 2016;365:153–9.
[25] Boinovich LB, Emelyanenko AM, Modestov AD, Domantovsky AG, Emelyanenko KA. Synergistic effect of superhydrophobicity and oxidized layers on corrosion resistance of aluminum alloy surface textured by nanosecond laser treatment. ACS Appl Mater Interfaces 2015;7(34):19500–8.
[26] Chen Tianchi GSLH. Laser-Induced superhydrophobic Ti-Ni shape memory alloy with corrosion resistance and self-cleaning properties. Journal of Laser Micro/Nanoengineering 2017;12(3).
[27] Yu Z, Xu Z, Guo Y, Xin R, Liu R, Jiang C, et al. Study on properties of SLM-NiTi shape memory alloy under the same energy density. J Journal of Materials Research and Technology 2021;13:241–50.
[28] Xu Z, Guo Y, Liu Y, Jia B, Sha P, Li L, et al. An extremely efficiency method to achieve stable superhydrophobicity on the surface of additive manufactured NiTi Alloys: "Ultrasonic Fluorination". Appl Surf Sci 2023;612.
[29] Yang K, Shi J, Wang L, Chen Y, Liang C, Yang L, et al. Bacterial anti-adhesion surface design: surface patterning, roughness and wettability: a review. J Mater Sci Technol 2022;99:82–100.
[30] Ta VD, Dunn A, Wasley TJ, Li J, Kay RW, Stringer J, et al. Laser textured surface gradients. Appl Surf Sci 2016;371:583–9.
[31] Yang Y, Ma Y, Li W, Ma L, Li Z, Jia B, et al. Anti-corrosion superhydrophobic surface of LPBF- NiTi alloy fabricated by nanosecond laser machining. Opt Laser Technol 2023;158.
[32] Huang XY, Ackland GJ, Rabe KM. Crystal structures and shape-memory behaviour of NiTi. Nat Mater 2003;2(5):307–11.
[33] Greczynski G, Hultman L. X-ray photoelectron spectroscopy: towards reliable binding energy referencing. Prog Mater Sci 2020;107.
[34] Ma Y, Jiang L, Hu J, Liu H, Wang S, Zuo P, et al. Multifunctional 3D micro-nanostructures fabricated through temporally shaped femtosecond laser processing for preventing thrombosis and bacterial infection. ACS Appl Mater Interfaces 2020;12(15):17155–66.
[35] Zhang BB, Qiu KJ, Wang BL, Li L, Zheng YF. Surface characterization and cell response of binary Ti-Ag alloys with CP Ti as material control. J Mater Sci Technol 2012;28(9):779–84.
[36] Lopez MF, Jimenez JA, Gutierrez A. XPS characterization of surface modified titanium alloys for use as biomaterials. Vacuum 2011;85(12):1076–9.
[37] Ye L, Yang C, Tian L, Zan L, Peng T. Tunable photocatalytic selectivity of fluoropolymer PVDF modified TiO2. Appl Surf Sci 2011;257(18):8072–7.
[38] Ryu W-H, Kim D-H, Kang S-H, Kwon H-S. Electrochemical properties of nanosized Li-rich layered oxide as positive electrode materials for Li-Ion batteries. RSC Adv 2013;3(22).
[39] Biesinger MC, Lau LW, Gerson AR, Smart RS. The role of the Auger parameter in XPS studies of nickel metal, halides and oxides. Phys Chem Chem Phys 2012;14(7):2434–42.
[40] Ravizza E, Spadoni S, Piagge R, Comite P, Wiemer C. XPS composition study of stacked Si oxide/Si nitride/Si oxide nano-layers. Surf Interface Anal 2012;44(8):1209–13.
[41] Radi A, Khalil-Allafi J, Heidarzadeh A, Yapici GG, Etminanfar MR, Mozafari SZ, et al. Effect of stress aging induced precipitates on corrosion behavior of NiTi shape memory alloys. Met Mater Int 2021;27(10):3968–74.
[42] Guo YT, Su YC, Jia SQ, Sun GX, Gu R, Zhu DH, et al. Hydroxyapatite/titania composite coatings on biodegradable magnesium alloy for enhanced corrosion resistance, cytocompatibility and antibacterial properties. J Electrochem Soc 2018;165(14):C962–72.
[43] Qiu P, Gao PP, Wang SY, Li ZH, Yang Y, Zhang QQ, et al. Study on corrosion behavior of the selective laser melted NiTi alloy with superior tensile property and shape memory effect. Corrosion Sci 2020;175.
[44] Deng J, Wang KS, Hu P, Zhou YH, Chang T, Hu BL, et al. Electrochemical behavior and microstructural characterization of lanthanum-doped titanium-zirconium-molybdenum alloy. J Alloys Compd 2018;763:687–94.
[45] Guo YT, Jia SQ, Qiao L, Su YC, Gu R, Li GY, et al. Enhanced corrosion resistance and biocompatibility of polydopamine/dicalcium phosphate dihydrate/collagen composite coating on magnesium alloy for orthopedic applications. J Alloys Compd 2020;817.
[46] Guo Y, Xu Z, Liu Y, Liu M, Sha P, Li L, et al. Achieving illustrious friction and corrosion resistance on a laser powder bed fusion nitinol rare earth alloy. Materials Today Advances 2023;17.